Extracting Snow Cover in Mountain Areas Based on SAR and Optical Data

Guangjun He, Pengfeng Xiao, *Member, IEEE*, Xuezhi Feng, Xueliang Zhang, Zuo Wang, and Ni Chen

Abstract—Snow cover in cold and arid regions is a key factor controlling regional energy balances, hydrological cycle, and water utilization. Interferometric synthetic aperture radar (InSAR) technology offers the ability to monitor snow cover in all weather. In this letter, a support vector machine (SVM) method for extracting snow cover based on SAR and optical data in rugged mountain terrain is introduced. In this method, RadarSat-2 InSAR interferometric coherence images are analyzed, adopting snow-covered and snow-free areas obtained from GF-1 satellite observations as the "ground truth." The analysis results indicate that the coherence in copolarizations is clearly correlated with the underlying surface type and local incidence angle. These two factors, combined with training samples from GF-1 wide field viewer data, were used to build an SVM to classify coherence images in HH polarization. The classification results demonstrate that snow cover extraction using this method can achieve mean accuracies of 83.8% and 77.5% in areas with low and high vegetation coverage, respectively. These accuracies are significantly higher than those achieved by the typical thresholding algorithm (72.7% and 69.2%, respectively).

Index Terms—Interferometric coherence, mountain areas, multisensor, snow cover extraction.

I. INTRODUCTION

SNOW is a crucial factor controlling both global and regional energy balances [1]. Moreover, snow cover offers valuable information in that it provides insight into the amount of water that can be expected to be available from snowmelt for runoff and water supply [2]. Recently, snow cover mapping based on optical remote sensing has become practical, owing particularly to the distinct spectral characteristics of snow [3]. However, it remains difficult to differentiate snow from cloud. In addition, for mountain areas, highly accurate digital elevation model (DEM) is required in terrain shadow detection and radiometric terrain correction [4]. In contrast, microwave remote sensing can be used to discriminate snow with other surfaces regardless of weather, time, and solar illumination conditions because of its high penetrability. However, the spatial resolution of current spaceborne passive microwave sensors is too coarse to provide the fine-resolution snow cover data required for snow cover monitoring in mountain areas [5]. Conversely, the spatial resolution of active microwave sensors, particularly synthetic aperture radar (SAR) sensors, is able to provide useful information at both the regional and drainage basin scales. Accordingly,

it can be used to complement optical remote sensing for snow cover mapping in rugged mountain terrain [6].

The currently available snow cover mapping techniques using SAR imagery can be grouped into four main categories. The first involves change detection based on multitemporal and single-polarization images. Because the backscattering of snow can be reduced by 3–4 dB at C-band during the time span required for snowmelt, wet snow cover can be extracted based on the changes in backscattering between a wet snow image and a reference image (either snow free or dry snow) [7]. The second technique is the multifrequency and multipolarization method. Shi and Dozier evaluated the characteristics of the backscattering, polarization, and frequency ratios of snow in SIR-C/X-SAR images and then developed two supervised classifiers based on a classification tree technique [8]. One of these classifiers utilized intensity measurements, polarization properties, and frequency ratios jointly, allowing discrimination between dry and wet snow, although this requires a highly accurate DEM for radiometric terrain correction. The other classifier was developed based on polarization properties and backscattering ratios between different frequencies. Recently, some snow classification methods (polarimetric decomposition, object-oriented image analysis, etc.) using the polarimetric SAR data have been explored [9], [10]. In brief, the radar penetration depth, depending on the frequency, can reach tens of meters for dry snow [11]. Unlike the X-band or higher frequencies with higher sensitivity to dry snow, the major scattering source at C-band is the snow–ground interface. This makes it difficult to acquire dry snow cover using C-band or lower frequencies. The third snow mapping technique involves the analysis of SAR and optical images individually before combining them to form a single snow cover product [12]. This product is controlled by a pixel-by-pixel confidence value that is computed for each image analyzed; the confidence algorithm may consider information about parameters such as local observation angle, clouds, and snow state, among others. Finally, the fourth snow mapping technique involves the measurement of interferometric coherence between two repeat passes [13], based on which a threshold slicing algorithm has been developed for mapping both dry and wet snow cover. Snow cover has a considerable impact on the interferometric coherence. However, snow-free surfaces preserve coherence before and after snowfall. Thus, the interferometric coherence of a snow-covered surface is lower than that of a snow-free surface, such that a reasonable threshold can typically be used to identify snow-covered areas [14], [15].

In general, SAR interferometry in mountain areas incorporates a number of factors related to the coherence value [16], including the underlying surface type and topographic effects; typically, these factors have not been taken into account in previous studies. Thus, to address this, this study aims to extract snow cover using interferometric coherence and optical data
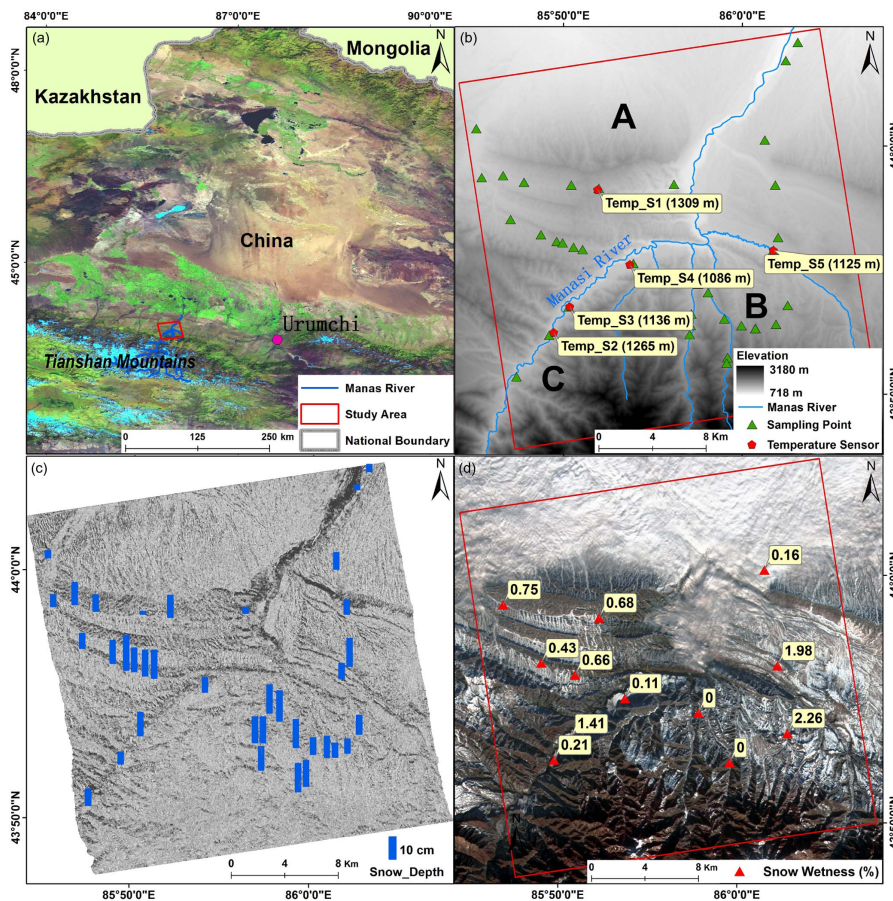
Fig. 1. Study area. (a) Location of the study area in Xinjiang Province, China. (b) DEM of the study area. (c) Coherence image of HH polarization of RadarSat-2. (d) WFV data of GF-1 satellite shown with a combination of green, red, and near-infrared bands.

while considering both underlying surface type and topographic effects.

II. STUDY AREA AND DATA

A. Study Area

The study area is located in the midstream of the Manas River on the north slope of the Tianshan Mountains in northwestern China [see Fig. 1(a)]. The elevation in the area ranges from 714 m on the piedmont slopes up to 3180 m in the mountain forests [see Fig. 1(b)]. Altitudinal zonation in mountain vegetation characteristics is apparent, with bare land and sparse vegetation at low altitudes (patch A), subshrubs and grass at moderate altitudes (patch B), and alpine meadow and spruce forest at high altitudes (patch C). The study area lies within the seasonal snow cover zone, where the snow accumulation period extends from November to February in the following year. Typically, the snow in this region begins to melt at the end of February or in early March.

B. Data

In this study, SAR and optical data were combined, considering in depth the spatial resolution of the data, the ease of data acquisition, and the snow accumulation period. In particular, repeat-pass RadarSat-2 data were selected to generate interferometric coherence images [see Fig. 1(c)]. Wide field viewer (WFV) data acquired on October 2, 2013, represent

TABLE I
CHARACTERISTICS OF OPTICAL AND SAR DATA

Data	Band (µm)	Acquisition time	Spatial resolution (m)
SAR data (RadarSat-2)	Band C Fine quad-pol	2013.10.02 18:16 2013.12.13 18:17	Range: 12 Azimuth: 8
Optical data (GF-1 WFV)	0.45–0.52 0.52–0.59 0.63–0.69 0.77–0.69	2013.10.02 13:04 2013.12.14 13:15	16

totally snow free condition and were used to obtain the underlying surface information. WFV data from December 14, 2013 [see Fig. 1(d)], were selected to delineate snow-covered and snow-free areas. The WFV sensor is a multispectral scanning radiometer on board the GF-1 satellite of China, launched on April 26, 2013, with a scanning swath of 800 km (combination of four WFV sensors) and a temporal resolution of four days. Additional parameters related to the data are listed in Table I.

Field work was performed during December 11–17, 2013, to understand the physical state of snow; 34 flat areas were selected [see Fig. 1(b)] to make vertical profiles of snow cover (snow pits). Fig. 1(c) shows the snow depth of each sampling point. A snow fork was used to measure the electrical parameters and liquid water content of snow [17]. Fig. 1(d) illustrates the snow wetness data at 2 cm below the snow surface. Five temperature sensors were placed at different elevations [see Fig. 1(b)] to record the air temperature every 10 min. Fig. 2
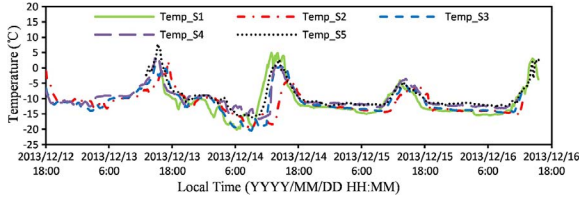
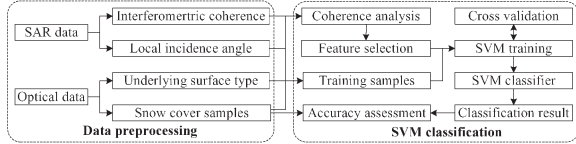Fig. 2. Changes of air temperature during *in situ* measurement.

Fig. 3. Schematic flowchart illustrating the snow cover extraction method adopted in this study.

illustrates the changes in air temperature that occurred during *in situ* measurement.

III. METHODOLOGY

A flowchart summarizing the method proposed in this study is presented in Fig. 3, which includes the following steps: data preprocessing, feature selection based on coherence analysis, snow cover extraction, and accuracy assessment.

A. Data Preprocessing

ENVI/SARScape software was used to process the SAR and optical data. First, RadarSat-2 raw data were processed to obtain single-look complex (SLC) data products. Coregistration of these products was performed using a maximum correlation algorithm with the ASTER GDEM V2 product. The fourth cubic convolution algorithm was selected to resample the precisely registered SLC data at a resolution of 16 m. Then, the baseline was estimated by taking the image from October 2, 2013, as the reference image and the other as the match image. The perpendicular baseline (161 m) was considered to be generated. Normalized difference vegetation index (NDVI) [18] was calculated using the WFV data from October 2, 2013. Supervised maximum-likelihood classification module of the software was used to obtain snow-covered and snow-free samples using the WFV data from December 14, 2013, from which the shadow and cloud regions had been manually removed to ensure the accuracy of the samples above 95%.

B. Feature Selection Based on Coherence Analysis

The coherence CC can be expressed as follows [16]:

$$CC = C_{in} \cdot C_{az} \cdot C_{no} \cdot C_{bl} \cdot C_{pr} \cdot C_{sp} \cdot C_{te} \qquad (1)$$

where C_{in} refers to the radar platform and accounts for differences in Doppler centroid frequency between interferometric SAR (InSAR) data pairs. C_{az} refers to the azimuth and can be obtained by calculating the Doppler frequency difference. C_{no} is the system thermal noise, including gain and antenna characteristics. C_{pr} refers to the data processing algorithm. C_{bl} is the baseline. C_{sp} denotes the sensor geometry effects that result from the orbit difference between the InSAR data pairs, which can be expressed as follows:

$$C_{sp} = 1 - \frac{2|B|R_y \cos^2 \theta}{\lambda r} \qquad (2)$$
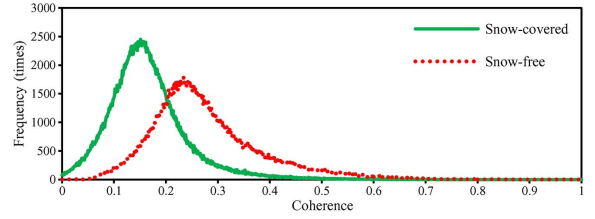

Fig. 4. Histograms of the coherence values for snow-covered and snow-free pixels from HH polarized InSAR data pairs.

where B is the baseline, R_y is the range resolution, λ is the radar wavelength, r is the distance from the sensor itself to the center of a resolution element, and θ is the sensor look angle. C_{te} denotes the temporal decorrelation caused by changes in the underlying surface, which is given as follows:

$$C_{te} = \exp \left\{ -\frac{1}{2} \left(\frac{4\pi}{\lambda} \right)^2 \left(T_y^2 \cos^2 \theta + T_Z^2 \cos^2 \theta \right) \right\} \qquad (3)$$

where T_y and T_z are the standard deviation in the range and height directions, respectively. Regardless of the effects of the radar platform and data processing algorithm, for the extraction of snow in mountain areas, the interferometric coherence is heavily dependent on two primary factors: underlying surface variation, including that associated with snow accumulation, snow melting, and vegetation growth, and the local incidence angle, in relation to topography.

The typical thresholding algorithm was built based on the assumption that the coherence variation is caused only by snow cover. Histograms were constructed (see Fig. 4) to illustrate the distribution of the coherence value for both snow-covered and snow-free pixels. The results reveal that a threshold of 0.21 was able to achieve maximum accuracy of only 71.6% when extracting snow cover using the thresholding algorithm.

To investigate the decorrelation caused by underlying surface changes, the underlying surface was divided into three types: mountain forest (MF), high vegetation coverage (HVC), and low vegetation coverage (LVC), according to a study on the NDVI image and land use map obtained from the land use database of China at the scale of 1:100 000. The MF areas were not considered in this study owing to the complexity of their decorrelation. To address the influence of local incidence angle in more detail, the average coherence values of selected snow-covered and snow-free pixels were calculated at an interval of 5° for each underlying surface type with local incidence angle in the range 0°–90° (see Fig. 5). In particular, the average coherence differences between snow-covered and snow-free pixels in HH and VV polarizations were found to be more significant than those for HV and VH polarizations, mainly because the backscattering intensity of copolarizations is higher than cross-polarizations under normal situations. Moreover, owing to the decorrelation caused by snow accumulation, the average coherence value of snow-covered areas was found to be significantly smaller than that for snow-free areas, particularly in HH and VV polarizations. For the underlying surface, the coherence loss of the HVC areas was high compared with the LVC areas in HH and VV polarizations, and the difference between HV and VH polarizations was not pronounced. Moreover, the average coherence values are clearly correlated to the local incidence angle in HH and VV polarizations, such that the coherence increases from 0° to 30° and decreases from 30° to 90°; similar relation was found between backscattering intensity and local incidence angle. Therefore, the coherence
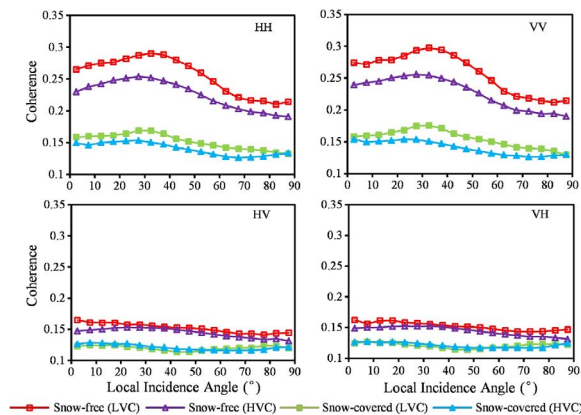
Fig. 5. Coherence value comparisons for snow-covered and snow-free pixels from HVC and LVC areas. Average local incidence angle serves as the x-axis, and average coherence serves as the y-axis.
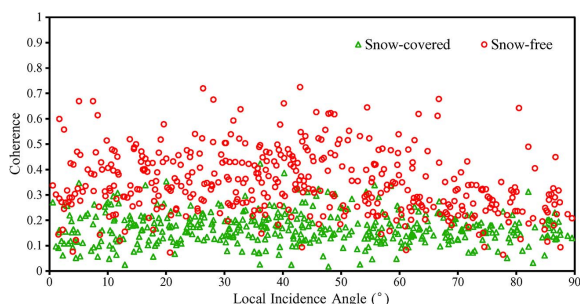

Fig. 6. Scatterplot of randomly selected pixels in the LVC area in the feature space consisting of coherence and local incidence angle.

value can be considered to be related to all of the following factors: polarization mode, underlying surface type, and local incidence angle. Accordingly, these parameters should be considered when extracting snow cover.

C. Snow Cover Extraction

Because the HH and VV polarizations exhibit greater coherence differences between snow-covered and snow-free pixels than the HV and VH polarizations, and the VV polarization exhibits the same coherence characteristics as the HH polarization, the HH polarization coherence image was selected for the extraction of snow cover. The HVC and LVC areas were separated for extraction, because the HVC areas exhibit higher decorrelation. Then, the feature space of each underlying surface type consisted of the coherence value for HH polarization and the local incidence angle. An example of LVC is presented in Fig. 6. Eight hundred pixels of snow-covered and snow-free areas in Fig. 6 were randomly selected based on the snow cover information discriminated by optical data. The distribution of these points indicates that a nonlinear classifier should be adopted to discriminate snow-covered from snow-free pixels.

The support vector machine (SVM) is a classifier that is used widely owing to its ability to solve nonlinear classification problems with small samples and high dimensions [19]. The SVM classifier is typically constructed based on a small number of training instance-label pairs, which are used to search for the support vectors and then to predict unknown data. For a two-class problem, it can be assumed that the training instance-label pairs are $\{(x_i, y_i), i = 1, \ldots, N\}$. Each training instance-label pair (x_i, y_i) is a vector in the d-dimensional feature space $x_i = [x_{i,1}, x_{i,2}, \ldots, x_{i,d}]^T$ with a corresponding

label y_i. The decision function in the kernel space can be expressed as follows:

$$f(x) = \sum_S a_i y_i K(x_i, x) + b \quad (4)$$

where $f(x)$ represents the margins. $S = \{i : 0 < a_i < C\}$, where C is a penalty parameter. Samples associated with nonzero a_i are so-called support vectors. b is a bias term that does not affect the performance significantly. $K(x_i, x)$ is the kernel function; in this study, a Gaussian RBF kernel was employed. This kernel took the following form:

$$K(x_i, x) = e^{-\gamma \|x_i - x\|^2} \quad (5)$$

where γ is a parameter that is inversely proportional to the width of the Gaussian kernel. The two parameters C and γ were not known beforehand, but grid-search and cross-validation methods were used to search for the best parameters [20]. Subsequently, the training instance-label pairs were used to confirm the support vectors.

Taking the LVC area as an example, there are 750 patterns from snow-covered areas and 750 patterns from snow-free areas. The patterns were divided into three subsets of equal size. Sequentially, one subset was used to test the classifier trained on the other two subsets. After the grid search conducted using threefold cross-validation, the best values of the two parameters were identified. Then, the classifier for the LVC areas was finally built. In addition, the SVM was trained for the overall (HVC and LVC areas together) to study the effects of underlying surface.

D. Accuracy Assessment

The extraction results were validated with high-resolution optical data, considering the optical data classification results as the "ground truth" data. The accuracies of the SVM method and the thresholding algorithm, which were used for the LVC and HVC areas, respectively, were calculated at intervals of $5°$ for local incidence angles in the range $0°$–$90°$. The accuracy calculation formula can be expressed as follows:

$$\text{Accuracy} = \frac{\text{OS\_SC} + \text{OS\_SF}}{\text{Total}} \cdot 100\% \quad (6)$$

where OS_SC and OS_SF are the numbers of pixels that were identified as snow covered and snow free, respectively, based on both the SVM method (i.e., the thresholding algorithm) and the optical data. Total denotes the number of valid pixels.

IV. RESULTS AND DISCUSSION

The accuracy assessment results are presented in Fig. 7. The mean accuracy of SVM trained for the HVC and LVC areas separately was found to be 83.8% for the LVC areas and 77.5% for the HVC areas; these values are slightly higher than the 81.2% and 75.2% accuracy of SVM trained for the overall and are considerably higher than the 72.7% and 69.2% accuracy achieved by the thresholding algorithm. Snow cover extraction results for the LVC and HVC areas are presented in Fig. 8.

The results indicate that the SVM method provides an effective means of extracting snow cover in mountain areas. By integrating the influences of local incidence angle and underlying surface, this method achieves improvements relative to the thresholding algorithm in the application of interferometric coherence. However, as shown in Fig. 7, the extracted snow
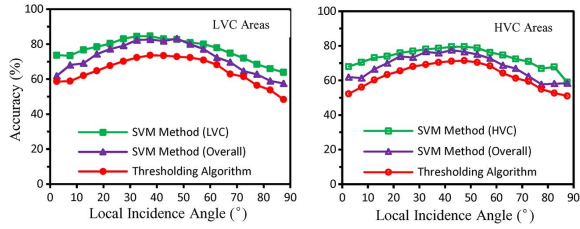
Fig. 7.   Accuracy comparison for the SVM method and the thresholding algorithm.
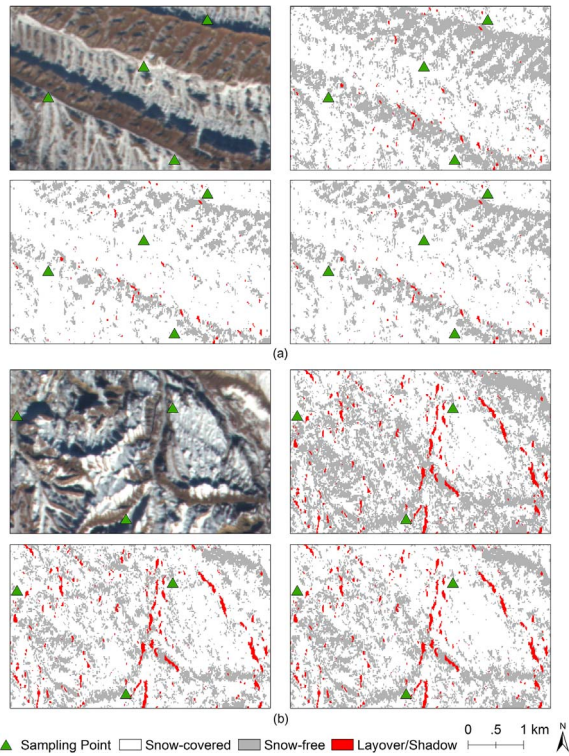

Fig. 8.   Snow cover extraction results for the (a) LVC areas and the (b) HVC areas. (Top left) Optical data. (Top right) Snow cover extraction results using the thresholding algorithm. (Bottom left) SVM trained for the overall. (Bottom right) SVM trained for the HVC and LVC areas separately.

cover is extremely patchy compared with the optical data. This may be because coherence is affected by other factors that were not considered in this study, including system thermal noise, the accuracy of DEM data, soil moisture variations, and the activity of humans and livestock. Moreover, the high dependence on prior information obtained from optical data could limit the utility of this newly proposed method. Nevertheless, this method has been shown to be useful for snow cover mapping in mountain areas when both SAR data and synchronous optical data are available.

V. CONCLUSION

A new approach based on SVM has been developed for snow cover extraction in mountain areas using combined SAR and optical data. In particular, the interferometric coherence value was studied in combination with factors such as polarization mode, underlying surface type, and local incidence angle. These factors were found to be closely related to the coherence value. SVM classifiers were constructed separately for the LVC and HVC areas, with regard to local incidence angle and coherence values as the feature space, and snow-covered and snow-free

areas were obtained from optical data as training samples. This newly developed method achieved extraction accuracy of 83.8% in the LVC areas and 77.5% in the HVC areas, offering significant improvements over the threshold slicing algorithm. In addition, snow in terrain shadows and cloud cover areas can be discriminated using this method. However, the proposed method highly depends on training samples, which is a general problem for supervised classification methods. Moreover, the accuracy of the SVM method is largely decided by the validity of the training samples. As a result, spatial resolution of the prior information should not be lower than the SAR data. Accordingly, future work should focus on reducing dependence on prior knowledge obtained from optical data.

REFERENCES

[1] T. P. Barnett, J. C. Adam, and D. P. Lettenmaier, "Potential impacts of a warming climate on water availability in snow-dominated regions," *Nature*, vol. 438, no. 7066, pp. 303–309, Nov. 2005.

[2] V. V. Salomonson and I. Appel, "Estimating fractional snow cover from MODIS using the normalized difference snow index," *Remote Sens. Environ.*, vol. 89, no. 3, pp. 351–360, Mar. 2004.

[3] D. K. Hall and G. A. Riggs, "Accuracy assessment of the MODIS snow products," *Hydrol. Process.*, vol. 21, no. 12, pp. 1534–1547, May 2007.

[4] D. Robinson, K. Kunzi, G. Kukla, and H. Rott, "Comparative utility of microwave and shortwave satellite data for all-weather charting of snow cover," *Nature*, vol. 312, no. 5993, pp. 434–435, Nov. 1984.

[5] J. C. Shi, Y. Du, and J. Y. Du, "Progresses on microwave remote sensing of land surface parameters," *Sci. China Earth Sci.*, vol. 55, no. 7, pp. 1052–1078, Jul. 2012.

[6] J. Koskinen *et al.*, "Snow monitoring using radar and optical satellite data," *Remote Sens. Environ.*, vol. 69, no. 1, pp. 16–29, Jul. 1999.

[7] T. Nagler and H. Rott, "Retrieval of wet snow by means of multitemporal SAR data," *IEEE Trans. Geosci. Remote Sens.*, vol. 38, no. 2, pp. 754–765, Mar. 2000.

[8] J. C. Shi and J. Dozier, "Mapping seasonal snow with SIR-C/X-SAR in mountainous areas," *Remote Sens. Environ.*, vol. 59, no. 2, pp. 294–307, Jan. 1997.

[9] L. Huang *et al.*, "Classification and snow line detection for glacial areas using the polarimetric SAR image," *Remote Sens. Environ.*, vol. 115, no. 7, pp. 1721–1732, Jul. 2011.

[10] S. E. Park, Y. Yamaguchi, and G. Singh, "Polarimetric SAR response of snow-covered area observed by multi-temporal ALOS PALSAR fully polarimetric mode," *IEEE Trans. Geosci. Remote Sens.*, vol. 52, no. 1, pp. 329–340, Jan. 2014.

[11] F. T. Ulaby and R. K. Moore, *Microwave Remote Sensing: Active and Passive. Volume 2: Radar Remote Sensing and Surface Scattering and Emission Theory*.   Reading, MA, USA: Addison-Wesley, 1982.

[12] R. Solberg *et al.*, "Multi-sensor and time-series approaches for monitoring of snow parameters," in *Proc. IEEE Int. Geosci. Remote Sens. Symp.*, Sep. 2004, vol. 3, pp. 1661–1666.

[13] J. C. Shi, S. Hensley, and J. Dozier, "Mapping snow cover with repeat pass synthetic aperture radar," in *Proc. IEEE Int. Geosci. Remote Sens. Symp.*, 1997, pp. 628–630.

[14] G. Luzi *et al.*, "Monitoring of an alpine glacier by means of groundbased SAR interferometry," *IEEE Geosci. Remote Sens. Lett.*, vol. 4, no. 3, pp. 495–499, Aug. 2007.

[15] V. Kumar and G. Venkataraman, "SAR interferometric coherence analysis for snow cover mapping in the western Himalayan region," *Int. J. Digit. Earth*, vol. 4, no. 1, pp. 78–90, Feb. 2011.

[16] H. A. Zebker and J. Villasensor, "Decorrelation in interferometric radar echoes," *IEEE Trans. Geosci. Remote Sens.*, vol. 30, no. 5, pp. 950–959, Sep. 1992.

[17] A. Sihvola and M. Tiuri, "Snow fork for field determination of the density and wetness profiles of a snow pack," *IEEE Trans. Geosci. Remote Sens.*, vol. GE-24, no. 5, pp. 717–721, Sep. 1986.

[18] J. W. Rouse, R. H. Haas, J. A. Schell, and J. C. Harlan, "Monitoring the vernal advancement of retrogradation of natural vegetation," NASA/GSFC, Type III, Final Report, Greenbelt, MD, USA, 1974.

[19] G. V. Camps and L. Bruzzone, "Kernel-based methods for hyperspectral image classification," *IEEE Trans. Geosci. Remote Sens.*, vol. 43, no. 6, pp. 1351–1362, Jun. 2005.

[20] Y. Bazi and F. Melgani, "Toward an optimal SVM classification system for hyperspectral remote sensing images," *IEEE Trans. Geosci. Remote Sens.*, vol. 44, no. 11, pp. 3374–3385, Nov. 2006.